How to cite: *Angew. Chem. Int. Ed.* **2023**, *62*, e202309351
doi.org/10.1002/anie.202309351

CO_2 Reduction Reaction | Hot Paper

Breaking K^+ Concentration Limit on Cu Nanoneedles for Acidic Electrocatalytic CO_2 Reduction to Multi-Carbon Products

Xin Zi[+], Yajiao Zhou[+], Li Zhu, Qin Chen, Yao Tan, Xiqing Wang, Mahmoud Sayed, Evangelina Pensa, Ramadan A. Geioushy, Kang Liu, Junwei Fu, Emiliano Cortés,* and Min Liu**

Abstract: Electrocatalytic CO_2 reduction reaction (CO_2RR) to multi-carbon products (C_{2+}) in acidic electrolyte is one of the most advanced routes for tackling our current climate and energy crisis. However, the competing hydrogen evolution reaction (HER) and the poor selectivity towards the valuable C_{2+} products are the major obstacles for the upscaling of these technologies. High local potassium ions (K^+) concentration at the cathode's surface can inhibit proton-diffusion and accelerate the desirable carbon-carbon (C–C) coupling process. However, the solubility limit of potassium salts in bulk solution constrains the maximum achievable K^+ concentration at the reaction sites and thus the overall acidic CO_2RR performance of most electrocatalysts. In this work, we demonstrate that Cu nanoneedles induce ultrahigh local K^+ concentrations (4.22 M) – thus breaking the K^+ solubility limit (3.5 M) – which enables a highly efficient CO_2RR in 3 M KCl at pH = 1. As a result, a Faradaic efficiency of 90.69 ± 2.15 % for C_{2+} (FE_{C2+}) can be achieved at 1400 mA.cm^{-2}, simultaneous with a single pass carbon efficiency (SPCE) of 25.49 ± 0.82 % at a CO_2 flow rate of 7 sccm.

Electrocatalytic CO_2 reduction to valuable fuels and chemicals enables CO_2 resource utilization through renewable clean electricity.[1–6] Among the CO_2 reduction products, multi-carbon products have drawn worldwide attentions due to their high energy density and market value.[7–12] Currently, most of the reported examples for the CO_2 reduction reaction (CO_2RR) to multi-carbon products (C_{2+}) are performed in alkaline or neutral electrolyte systems,[13–19] expecting to improve the selectivity of C_{2+} products by inhibition of the HER.[20–25] However, this strategy suffers from the low utilization of CO_2 due to its conversion into carbonates (CO_3^{2-}) when employing alkaline or neutral electrolytes.[26–28] For example, every two CO_2 molecules that react to obtain one C_2H_4 molecule, six CO_2 molecules are converted to CO_3^{2-}. This means that the maximum theoretical single-pass carbon efficiency is only 25 % with 100 % selectivity of C_2H_4 in a neutral electrolyte.[27] Due to the presence of abundant protons, the acidic electrolyte can avoid the formation of refractory CO_3^{2-}, then greatly improving the utilization rate of CO_2.[12] However, high proton concentration in acidic electrolyte easily leads to the undesired HER, reducing the C_{2+} product selectivity, which limits the applications of acidic CO_2RR.[29–31]

The alkali cations in acidic electrolyte, especially K^+, have been shown to effectively inhibit HER, and optimize the C–C coupling process for higher selectivity of multi-carbon products.[26–28] Gu et al.[27] reported that the adsorption of K^+ prevented the migration of protons from the diffusion layer to the catalyst surface, causing a local OH^- environment to inhibit HER. Huang et al.[32] found that K^+ can trigger CO_2 activation under a proton-depletion local OH^- environment. Zhao et al.[33] reported that a K^+-enriched environment promoted C–C coupling processes, leading to higher efficiencies for C_{2+} products. The high K^+ concentration is therefore advantageous, and how to increase the local K^+ concentration on the electrode's surface becomes an important strategy for optimizing acidic CO_2RR.

[*] X. Zi,[+] Y. Zhou,[+] Q. Chen, Y. Tan, X. Wang, Dr. K. Liu, Dr. J. Fu, Prof. M. Liu
Hunan Joint International Research Center for Carbon Dioxide Resource Utilization, School of Physics, Central South University
Changsha 410083, Hunan (P. R. China)
E-mail: fujunwei@csu.edu.cn
minliu@csu.edu.cn

L. Zhu, Dr. E. Pensa, Prof. E. Cortés
Nanoinstitut München, Fakultät für Physik, Ludwig-Maximilians-Universität München
80539 München (Germany)
E-mail: Emiliano.Cortes@lmu.de

Dr. M. Sayed
Chemistry Department, Faculty of Science, Fayoum University
Fayoum 63514 (Egypt)

Dr. R. A. Geioushy
Central Metallurgical Research and Development Institute, CMRDI
P.O. Box: 87 Helwan 11421, Cairo (Egypt)

[+] These authors contributed equally to this work.

Using an electrolyte with high concentration of potassium salt to provide high K^+ concentration is simple and effective. However, severe salting-out effect by high concentration of potassium salt will block the gas channel of the reactor, and cause a device failure. Moreover, restricted by the solubility of potassium salts in the bulk electrolyte, the concentration limit of K^+ in a bulk KCl solution is ≈3.5 M at normal temperature and pressure.[34] In 2016, Liu et al.[35] proposed that local electric fields can induce a K^+-concentration effect. At that time, it was shown that a high curvature Au-nanoneedle electrode generates a strong local electric field confinement that enables the K^+ concentration at the surface of the electrode. Inspired by the field-induced K^+ concentration effect, we expect to break the solubility limit of K^+ through the enrichment of K^+ on the surface of a copper nanoneedle (CuNNs) catalyst with high curvature structure.[36] This route may assist in the generation of highly selective multi-carbon products (C_{2+}) with high current density in acidic electrolyte.

In this work, CuNNs catalysts were prepared on polytetrafluoroethylene (PTFE) substrate with a copper conductive layer. The CO_2RR performance was tested in a flow cell, 3 M KCl solution at pH = 1 was selected as electrolyte. Finite element simulations (COMSOL) proved that the high-curvature Cu nanoneedle structure induces a strong local electric field, promoting K^+ accumulation on the catalyst surface. The local K^+ concentration at the surface of the CuNNs can be as high as 4.22 M in 3 M KCl electrolyte, which greatly exceeds the dissolution limit of KCl in bulk electrolyte (3.5 M). Moreover, we confirm that the K^+-enriched local environment reduces the energy barrier of C–C coupling. As a result, the CuNNs catalysts achieve a 90.69 ± 2.15 % Faradaic efficiency for C_{2+} products at 1400 mA cm^{-2} in acidic electrolyte (pH = 1), exceeding the reported efficiencies so far for acidic CO_2RR. The single pass carbon efficiency (SPCE) reaches 25.49 ± 0.82 % at CO_2 flow rate of 7 sccm, which is exceed to the maximum theoretical value of 25 % for 100 % C_2H_4 selectivity in neutral electrolyte. This work provides a new strategy for improving the selectivity of C_{2+} at high current density in strong acidic electrolyte.

Finite Element Simulations. COMSOL Multiphysics simulations were used to investigate the reaction microenvironment of the CuNNs and the Cu film. The details are shown in the Simulation section of the Supporting Information. The distribution of electric field (shown in Figure 1a) indicates that the high curvature of the nanoneedle can induce high-intensity electric field near the tip, specifically up to 1.19×10^8 V m^{-1}. With such strong local electric field, the positively charged K^+ ions accumulate in the near-surface region of the tip (Figure 1b). In contrast, there is no significant enhancement of electric field intensity or K^+ concentration near the surface of the Cu film (Figures S1 and S2). We calculated the values of the K^+ concentrations near the tip of CuNNs and the surface of Cu film in bulk solutions with different K^+ concentrations. As shown in Figure 1c, the local K^+ concentration near the electrode surface increases approximately linearly as the bulk K^+ concentration increases. When the bulk K^+ concentration is

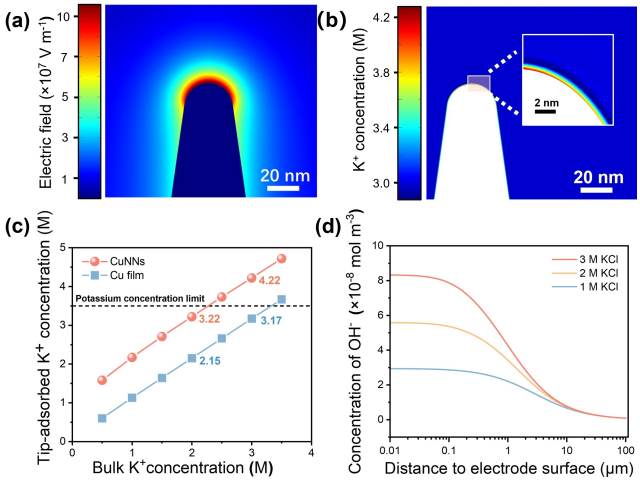

Figure 1. The surface microenvironment of catalyst investigated by COMSOL simulations. (a) Electric field distribution near the surface of CuNNs. (b) The K^+ concentration distribution on the surface of CuNNs in 3 M KCl. White color indicates the absence of K^+ ions. (c) The surface- adsorbed K^+ concentration of CuNNs and a Cu film in the bulk electrolyte with different K^+ concentrations. The dashed line is K^+ concentration limit. (d) The concentration profile of OH^- near the surface of the catalyst in the bulk electrolyte with different K^+ concentrations

2 M, the surface-adsorbed K^+ concentration at the Cu film is only 2.15 M. In contrast, the CuNNs exhibit a significantly higher concentration of 3.22 M at the tip needle, approaching the dissolution limit of KCl (3.5 M). Furthermore, increasing the bulk K^+ concentration to 3 M results in a remarkable tip-adsorbed K^+ concentration of 4.22 M on the Cu nanoneedle, exceeding the solubility limit of KCl. These results demonstrate the effective ability of CuNNs to enhance the local concentration of K^+ ions, surpassing the limiting concentration. Consequently, the utilization of unsaturated KCl electrolytes (such as 3 M, mitigating the salting effect), holds promise for ultrahigh local K^+ concentration to expedite the carbon-carbon (C–C) coupling process and inhibit the proton diffusion to the surface.

To investigate the impact of K^+ ions on inhibiting the HER, we conducted simulations to analyze the distribution of OH^- concentration in the near-surface region at various bulk K^+ concentrations. Figure 1d shows that the OH^- concentration is high in the proximity of the electrode surface, which can be attributed to the sluggish diffusion of protons caused by the presence of a high local K^+ concentration. Furthermore, there is a linear correlation between the local OH^- concentration and the K^+ one near the catalyst surface, indicating that higher amounts of K^+ ions result in a more pronounced OH^- concentration at the electrode surface. These simulation findings highlight the considerable potential of CuNNs in suppressing the HER in acidic electrolytes.

Structure and Morphology Characterization. CuNNs catalysts were fabricated using vacuum thermal evaporation and electrodeposition methods on PTFE substrates, as the porous nature of PTFE enables it to act as a gas diffusion

electrode in flow cells. The process involved initially depositing a conductive Cu layer onto PTFE through vacuum thermal vapor deposition, followed by electrodeposition of Cu dendrites with a nanoneedle structure (CuNNs) onto the Cu-coated PTFE substrate (Figure 2a). For comparison, the Cu-coated PTFE substrate directly acted as a Cu film catalyst, and the Cu nanoparticle (CuNPs) was prepared by a similar preparation method to CuNNs. The XRD patterns (Figure 2b) indicate that CuNNs, CuNPs, and the Cu film on PTFE share the same Cu diffraction peaks.[37] The XPS spectra (Figure S3) show two major peaks at 952 and 932 eV, ascribed to Cu^{+}/Cu^{0} species. Therefore, it can be concluded that these catalysts have the same composition.

As shown in Figures 2c-d, the Cu film exhibits a flat morphology with uniformly sized nanoparticles and the CuNPs exhibits large copper nanoparticles. In contrast, Figure 2e illustrates that CuNNs consist of a dendritic copper framework with nanoneedle structures. The corresponding elemental mapping using energy dispersive spectroscopy (EDS) (Figures S4 and S5) confirms that Cu is the major component, while small amounts of O are also present due to slight surface oxidation. Furthermore, a magnified TEM image of CuNNs (Figure 2f) reveals the pronounced curvature of the copper needles. The curvature (κ) of the nanoneedle can be determined to be approximately 0.067 nm^{-1} from a high-angle annular dark-field scanning TEM (HAADF-STEM) image (Figure 2g). This single nanoneedle structure aligns with the model constructed in COMSOL Multiphysics simulations.

Local K^{+} concentration and C–C coupling energy barrier. To investigate the adsorption capacity of K^{+}, we conducted K^{+} adsorption tests on CuNNs, CuNPs, and Cu film under different K^{+} concentration electrolytes, with applied potential (Figure 3a). The detailed methodology can be found in the Supporting Information. As depicted in Figure 3b, the local adsorbed K^{+} concentration at CuNNs consistently exceeded that at CuNPs and Cu film, across various bulk K^{+} concentrations. Remarkably, at the bulk K^{+} concentration of 3 M, CuNNs exhibited over 4 times higher

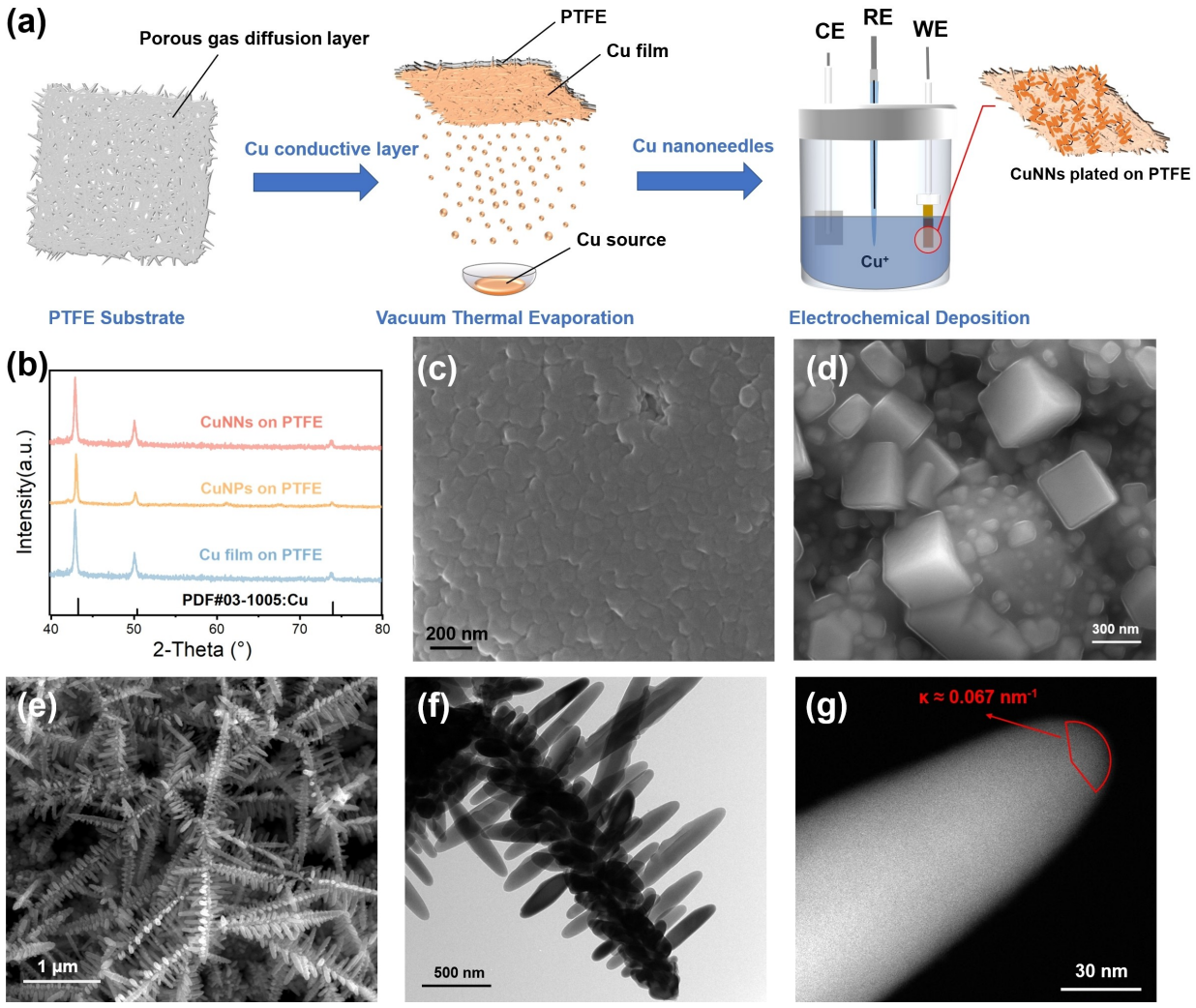

Figure 2. (a) A Scheme of the synthesis process of CuNNs. (b) XRD patterns of CuNNs, CuNPs, and Cu film on PTFE substrate. (c-e) SEM images of Cu film, CuNPs and CuNNs, respectively. (f) TEM image of CuNNs. (g) HAADF-STEM image of a single nanoneedle from the CuNNs.

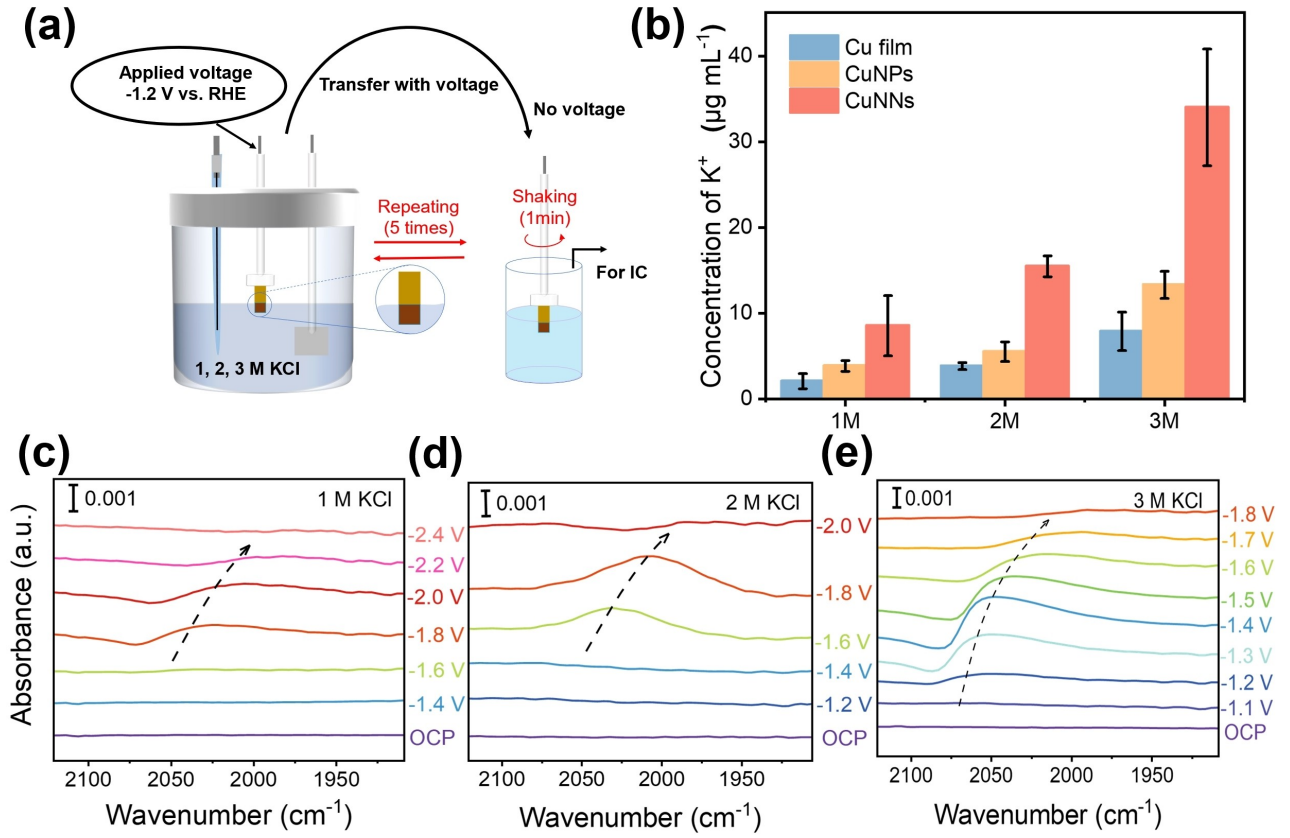

Figure 3. (a) Schematic diagram illustrating the determination of adsorbed-K^+ concentration at the electrode surface using ion chromatography (IC). (b) Comparison of the adsorbed-K^+ concentration on Cu film, CuNPs, and CuNNs at various K^+ bulk concentrations. (c–e) In situ attenuated total reflection FTIR spectra obtained on CuNNs at different applied potentials and with different K^+ bulk concentrations: (c) 1 M KCl, (d) 2 M KCl, and (e) 3 M KCl (Potentials vs. Ag/AgCl).

K^+ adsorption compared to the Cu film, highlighting the significantly enhanced K^+ adsorption capability of CuNNs.

Density functional theory (DFT) calculations were employed to determine the C–C coupling energy barrier on the Cu (100) surface for different amounts of adsorbed *CO and K^+. The results obtained from these calculations (Figure S6) reveal that an increase in the number of adsorbed K^+ and *CO species leads to a decrease in the energy barrier for C–C coupling. Interestingly, the energy barrier of C–C coupling is found to be more sensitive to the amount of adsorbed K^+ than *CO. This suggests that the K^+-promoted adsorption of *CO intermediates play a crucial role in reducing the energy barrier for C–C coupling.

To investigate the impact of enriched K^+-CuNNs catalyst for the CO_2 reduction to C_{2+}, we conducted in situ attenuated total reflection FTIR measurements on CuNNs immersed in electrolytes with different K^+ concentrations (Figure S7). As shown in Figures 3c-e, the typical bands ascribed to CO linear stretching (CO_L) in the spectral range of 1950 to 2100 cm^{-1} are observed.[38–42] When the potential is relatively low, the intensity of the CO band increased proportionally with the applied potential, indicating that *CO adsorption takes place at the catalyst surface. At higher applied potential, the intensity of the *CO band gradually decreased due to the C–C coupling (*CO dimerization). The onset potentials for *CO adsorption were determined to be −1.8, −1.6, and −1.2 V (vs. Ag/AgCl), while the potentials corresponding to the *CO depletion signal were found to be −2.2, −2.0, and −1.6 V (vs. Ag/AgCl) for electrolytes with concentrations of 1 M, 2 M, and 3 M, respectively (Figures 3c–e). These findings suggest that the presence of K^+ ions promote the reduction of CO_2 to *CO and facilitates the process of *CO dimerization. Consequently, it is reasonable to conclude that an increased K^+ concentration on the catalyst surface enhances the generation of *CO species and ultimately promotes the formation of C_{2+} products.[43–44]

Electrochemical CO_2RR in acidic electrolyte. The LSV curves of CuNNs and Cu film were obtained in various bulk concentrations of K^+ solutions while CO_2 was bubbled. As depicted in Figure S8, the onset potentials for CuNNs were found to be more positive compared to those for Cu film, and the reduction current density for CuNNs was higher than that for Cu film. These observations indicate that CuNNs possess a stronger ability for CO_2 reduction. Additionally, it was observed that the current density of CuNNs exhibited greater sensitivity to the K^+ concentration, implying that higher K^+ concentrations have a significant promoting effect on the CO_2 reduction reaction. These

findings further support the role of high K^+ concentrations in enhancing CO_2RR.

Next, we carried out electrocatalytic CO_2RR measurements on CuNNs, CuNPs and Cu film using electrolytes with different K^+ concentrations in a flow cell. Figures 4a–c show the product distributions obtained for CuNNs, CuNPs and Cu film in 3 M KCl solution at pH = 1 (the detailed values shown in Figures S9–S11). For CuNNs, the main products of CO_2RR are multi-carbon products (C_{2+}), such as ethylene, ethanol, and acetic acid. The FE of the C_1 product gradually decreases with increasing current density, while the FE_{C2+} increases. Remarkably, CuNNs exhibit an FE_{C2+} exceeding 80 % over a wide range of current densities (1000 - 1600 mA cm^{-2}), with the highest FE_{C2+} reaching 90.69 ± 2.15 % at 1400 mA cm^{-2}. These results significantly outperform similar CO_2RR studies conducted in acidic media. Furthermore, CuNNs display a significant suppression of H_2 production (FE_{H2} values below 5 % for 800–1200 mA cm^{-2}), whereas H_2 is the predominant product for CuNPs and Cu film (about 70 % at 1000 mA cm^{-2}). In addition, CuNNs were tested under weakly acidic condition (pH = 3.9) and near neutral condition (pH = 8.0) (Figures S12 and S13).

Considering the results obtained from COMSOL simulations, we can infer that the ability of CuNNs to concentrate K^+ contributes to their remarkable performance in CO_2RR. To further explore the influence of K^+, we conducted CO_2RR tests on CuNNs using electrolytes with varying K^+ concentrations. Figure 4d shows the relationship between the current density of C_{2+} and the applied voltage for CuNNs. The data clearly demonstrates that higher K^+ concentrations result in higher current densities of C_{2+} at the same applied potential, indicating that K^+ enhances the kinetic process of CO_2RR, specifically promoting the production of C_{2+} products.

We further assessed the performance of CuNNs by evaluating the current density of C_{2+} and the single-pass carbon efficiency (SPCE) at a fixed current density of 800 mA cm^{-2} and various CO_2 flow rates in a 3 M KCl solution with pH = 1. As depicted in Figure 4e, when the CO_2 flow rate exceeded 10 sccm (mL min^{-1}), the current density of C_{2+} surpassed 600 mA cm^{-2}. However, as the CO_2 flow rate decreases, the CO_2RR performance drops due to the lack of CO_2 supply. Interestingly, the SPCE exhibited an upward trend with decreasing CO_2 flow rate, reaching 25.49 ± 0.82 % at a flow rate of 7 sccm. This value is exceeded to the theoretically expected SPCE of 25 % for 100 % ethylene selectivity in neutral media.

To assess the stability of CuNNs, we conducted long-term CO_2RR tests at a constant current density of 800 mA cm^{-2} in a 3 M KCl solution with pH = 1. The results (Figure S14) demonstrate that the current density of C_{2+} remained stable at 450 mA cm^{-2} even after 8 hours of continuous CO_2RR, with the applied voltage maintained at −1.6 V vs. RHE. In addition, stability at higher current density was also tested. Under the current density of 1200 mA cm^{-2}, CuNNs can still maintain a current density of more than 600 mA cm^{-2} in 5 hours (Figure S15).

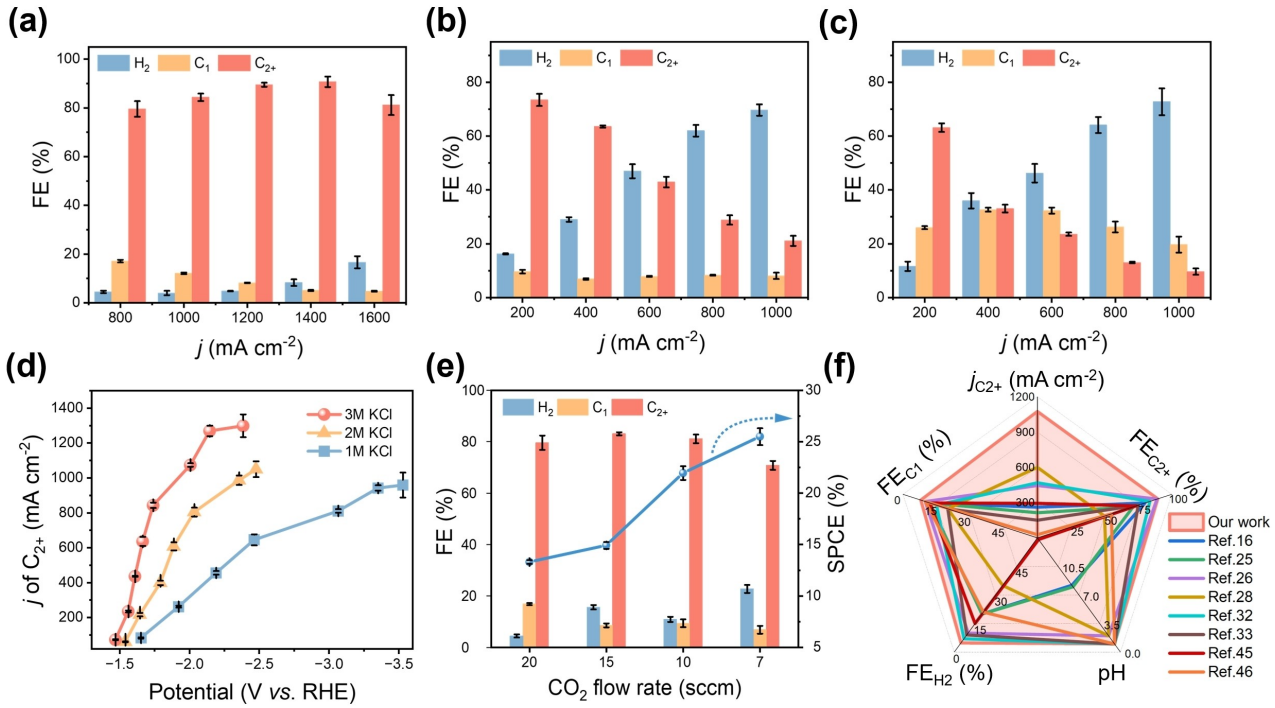

Figure 4. The CO_2RR product distributions obtained at different current densities for (a) CuNNs, (b) CuNPs and (c) Cu film. (d) The current density of C_{2+} at different applied voltages in the bulk electrolyte with different K^+ concentrations. (e) FE and SPCE of C_{2+} products obtained for CuNNs at 800 mA cm^{-2} using different CO_2 gas flow rates. (f) Comparison of FE_{C2+}, FE_{C1}, FE_{H2}, the current density of C_{2+}, and the bulk pH with other reported CO_2RR systems.

Finally, when comparing the performance of similar catalysts for CO_2RR in acidic media (details provided in Table S1), CuNNs exhibited outstanding characteristics, including high selectivity towards C_{2+} products, inhibition of HER and high current density of C_{2+} in highly acidic conditions (Figure 4f).[45–46]

In summary, CuNNs catalysts with nanoneedle structure were used for the electrocatalytic CO_2RR in acidic electrolytes. Compared to a Cu film, the high-intensity local electric field of the CuNNs tips induce ultrahigh K^+ concentration in 3 M KCl at pH = 1, breaking the dissolution limit of bulk K^+ solutions. As the K^+ concentration increases, the concentration of OH^- also increases in the region close to the electrode surface (due to charge neutrality), leading to the inhibition of the HER in acidic media. Moreover, the energy barrier for C–C coupling decreases with the high local K^+ concentration. The optimized CO_2RR performance of CuNNs in acidic electrolyte achieved a FE_{C2+} of 90.69 ± 2.15 % at 1400 mA cm^{-2} with a FE_{H2} below 5 %. At 800 mA cm^{-2}, the SPCE reaches 25.49 ± 0.82 % at a CO_2 flow rate of 7 sccm. This work confirms the great potential of ultrahigh local K^+ concentration for CO_2RR in acidic media.

Acknowledgements

The authors gratefully thank the Natural Science Foundation of China (Grant No. 22002189), Central South University Research Programme of Advanced Interdisciplinary Studies (Grant No. 2023QYJC012), Central South University Innovation-Driven Research Programme (Grant No. 2023CXQD042). The authors also acknowledge the funding and support from the Deutsche Forschungsgemeinschaft (DFG, German Research Foundation) under Germany's Excellence Strategy-EXC 2089/1-390776260 and the e-conversion research cluster, the Bavarian Program Solar Energies Go Hybrid (SolTech), the Center for NanoScience (CeNS), and the European Commission through the ERC Starting Grant CATALIGHT (802989). We are grateful for resources from High Performance Computing Center of Central South University. Open Access funding enabled and organized by Projekt DEAL.

Conflict of Interest

The authors declare no conflict of interest.

Data Availability Statement

The data that support the findings of this study are available from the corresponding author upon reasonable request.

Keywords: C–C Coupling · CO_2 Reduction · Cu Nanoneedles · Field Effect · K^+ Concentration

[1] S. Nitopi, E. Bertheussen, S. B. Scott, X. Liu, A. K. Engstfeld, S. Horch, B. Seger, I. E. Stephens, K. Chan, C. Hahn, *Chem. Rev.* **2019**, *119*, 7610–7672.
[2] J. Fu, K. Jiang, X. Qiu, J. Yu, M. Liu, *Mater. Today* **2020**, *32*, 222–243.
[3] J. Zhang, J. Fu, K. Dai, *J. Mater. Sci. Technol.* **2022**, *116*, 192–198.
[4] J. Fu, K. Liu, H. Li, J. Hu, M. Liu, *Environ. Chem. Lett.* **2022**, *20*, 243–262.
[5] F. Y. Gao, S. J. Hu, X. L. Zhang, Y. R. Zheng, H. J. Wang, Z. Z. Niu, P. P. Yang, R. C. Bao, T. Ma, Z. Dang, Y. Guan, X. S. Zheng, X. Zheng, J. F. Zhu, M. R. Gao, S. H. Yu, *Angew. Chem. Int. Ed.* **2020**, *59*, 8706–8712.
[6] L. Liu, T. Hu, K. Dai, J. Zhang, C. Liang, *Chin. J. Catal.* **2021**, *42*, 46–55.
[7] K. Jiang, Y. Huang, G. Zeng, F. M. Toma, W. A. Goddard III, A. T. Bell, *ACS Energy Lett.* **2020**, *5*, 1206–1214.
[8] J. Chen, S. Chen, Y. Li, X. Liao, T. Zhao, F. Cheng, H. Wang, *Small* **2022**, *18*, e2201633.
[9] C. Guo, Y. Guo, Y. Shi, X. Lan, Y. Wang, Y. Yu, B. Zhang, *Angew. Chem. Int. Ed.* **2022**, *61*, e202205909.
[10] P. Iyengar, M. J. Kolb, J. R. Pankhurst, F. Calle-Vallejo, R. Buonsanti, *ACS Catal.* **2021**, *11*, 4456–4463.
[11] H. Li, H. Zhou, Y. Zhou, J. Hu, M. Miyauchi, J. Fu, M. Liu, *Chin. J. Catal.* **2022**, *43*, 519–525.
[12] A. Ozden, J. Li, S. Kandambeth, X.-Y. Li, S. Liu, O. Shekhah, P. Ou, Y. Zou Finfrock, Y.-K. Wang, T. Alkayyali, F. Pelayo García de Arquer, V. S. Kale, P. M. Bhatt, A. H. Ip, M. Eddaoudi, E. H. Sargent, D. Sinton, *Nat. Energy* **2023**, *8*, 179–190.
[13] Q. Wang, K. Liu, K. Hu, C. Cai, H. Li, H. Li, M. Herran, Y. R. Lu, T. S. Chan, C. Ma, J. Fu, S. Zhang, Y. Liang, E. Cortes, M. Liu, *Nat. Commun.* **2022**, *13*, 6082.
[14] L. Zhu, Y. Lin, K. Liu, E. Cortés, H. Li, J. Hu, A. Yamaguchi, X. Liu, M. Miyauchi, J. Fu, M. Liu, *Chin. J. Catal.* **2021**, *42*, 1500–1508.
[15] W. Rong, H. Zou, W. Zang, S. Xi, S. Wei, B. Long, J. Hu, Y. Ji, L. Duan, *Angew. Chem. Int. Ed.* **2021**, *60*, 466–472.
[16] H. Wu, J. Li, K. Qi, Y. Zhang, E. Petit, W. Wang, V. Flaud, N. Onofrio, B. Rebiere, L. Huang, C. Salameh, L. Lajaunie, P. Miele, D. Voiry, *Nat. Commun.* **2021**, *12*, 7210.
[17] K. D. Yang, W. R. Ko, J. H. Lee, S. J. Kim, H. Lee, M. H. Lee, K. T. Nam, *Angew. Chem. Int. Ed.* **2017**, *56*, 796–800.
[18] Y. Zhou, F. Che, M. Liu, C. Zou, Z. Liang, P. De Luna, H. Yuan, J. Li, Z. Wang, H. Xie, *Nat. Chem.* **2018**, *10*, 974–980.
[19] R. Yang, J. Duan, P. Dong, Q. Wen, M. Wu, Y. Liu, Y. Liu, H. Li, T. Zhai, *Angew. Chem. Int. Ed.* **2022**, *61*, e202116706.
[20] G. Chen, J. Fu, B. Liu, C. Cai, H. Li, Z. Zhang, K. Liu, Z. Lin, M. Liu, *Environ. Sci.-Nano* **2022**, *9*, 3312–3317.
[21] X. Zhang, Y. Zhou, H. Zhang, H. Li, K. Liu, H. Li, H. Pan, J. Hu, J. Fu, S. Chen, M. Liu, *J. Energy Chem.* **2021**, *63*, 625–632.
[22] P. An, L. Wei, H. Li, B. Yang, K. Liu, J. Fu, H. Li, H. Liu, J. Hu, Y.-R. Lu, *J. Mater. Chem. A* **2020**, *8*, 15936–15941.
[23] T. M. Tang, Z. L. Wang, J. Q. Guan, *Adv. Funct. Mater.* **2022**, *32*, 2111504.
[24] M. H. Li, Y. Y. Ma, J. Chen, R. Lawrence, W. Luo, M. Sacchi, W. Jiang, J. P. Yang, *Angew. Chem. Int. Ed.* **2021**, *60*, 11487–11493.
[25] J. Zhang, W. Luo, A. Züttel, *J. Catal.* **2020**, *385*, 140–145.
[26] Y. Xie, P. Ou, X. Wang, Z. Xu, Y. C. Li, Z. Wang, J. E. Huang, J. Wicks, C. McCallum, N. Wang, Y. Wang, T. Chen, B. T. W. Lo, D. Sinton, J. C. Yu, Y. Wang, E. H. Sargent, *Nat. Catal.* **2022**, *5*, 564–570.
[27] J. Gu, S. Liu, W. Ni, W. Ren, S. Haussener, X. Hu, *Nat. Catal.* **2022**, *5*, 268–276.

[28] J. E. Huang, F. Li, A. Ozden, A. Sedighian Rasouli, F. P. García de Arquer, S. Liu, S. Zhang, M. Luo, X. Wang, Y. Lum, Y. Xu, K. Bertens, R. K. Miao, C.-T. Dinh, D. Sinton, E. H. Sargent, *Science* **2021**, *372*, 1074–1078.
[29] X.-B. Li, C.-H. Tung, L.-Z. Wu, *Angew. Chem. Int. Ed.* **2019**, *58*, 10804–10811.
[30] J. Wang, T. Xia, L. Wang, X. Zheng, Z. Qi, C. Gao, J. Zhu, Z. Li, H. Xu, Y. Xiong, *Angew. Chem. Int. Ed.* **2018**, *57*, 16447–16451.
[31] H. Gao, K. Liu, T. Luo, Y. Chen, J. Hu, J. Fu, M. Liu, *Chin. J. Catal.* **2022**, *43*, 832–838.
[32] Z. Ma, Z. Yang, W. Lai, Q. Wang, Y. Qiao, H. Tao, C. Lian, M. Liu, C. Ma, A. Pan, H. Huang, *Nat. Commun.* **2022**, *13*, 7596.
[33] Z. Yong, H. Long, O. Adnan, L. Shijie, K. M. Rui, O. Pengfei, A. Tartela, Z. Shuzhen, N. Jing, L. Yongxiang, X. Yi, F. Mengyang, C. Yuanjun, E. H. Jianan, X. Ke, Z. Jinqiang, P. O. B. Colin, Fengwang, E. H. Sargent, S. David, *Nat. Synth.* **2023**, *2*, 403–412.
[34] S. Bai, M. Song, T. Ma, F. Wang, Y. Liu, L. Guo, *Appl. Catal. B* **2023**, *323*, 122166.
[35] M. Liu, Y. Pang, B. Zhang, P. De Luna, O. Voznyy, J. Xu, X. Zheng, C. T. Dinh, F. Fan, C. Cao, *Nature* **2016**, *537*, 382–386.
[36] Y. Zhou, Y. Liang, J. Fu, K. Liu, Q. Chen, X. Wang, H. Li, L. Zhu, J. Hu, H. Pan, M. Miyauchi, L. Jiang, E. Cortes, M. Liu, *Nano Lett.* **2022**, *22*, 1963–1970.
[37] R. Betancourt-Galindo, P. Reyes, B. Puente-Urbina, C. Avila-Orta, O. Rodríguez-Fernández, G. Cadenas-Pliego, R. Lira-Saldivar, L. García-Cerda, *J. Nanomater.* **2013**, *5*, 980545.
[38] A. S. Malkani, J. Li, J. Anibal, Q. Lu, B. Xu, *ACS Catal.* **2020**, *10*, 941–946.
[39] A. Wuttig, C. Liu, Q. Peng, M. Yaguchi, Y. Surendranath, *ACS Cent. Sci.* **2016**, *2*, 522–528.
[40] W. Shan, R. Liu, H. Zhao, Z. He, Y. Lai, S. Li, G. He, J. Liu, *ACS Nano* **2020**, *14*, 11363–11372.
[41] E. Borguet, H. L. Dai, *J. Chem. Phys.* **1994**, *101*, 9080–9095.
[42] Y. Katayama, F. Nattino, L. Giordano, J. Hwang, R. R. Rao, O. Andreussi, N. Marzari, Y. Shao-Horn, *J. Phys. Chem. C* **2019**, *123*, 5951–5963.
[43] S. Sultan, H. Lee, S. Park, M. M. Kim, A. Yoon, H. Choi, T.-H. Kong, Y.-J. Koe, H.-S. Oh, Z. Lee, H. Kim, W. Kim, Y. Kwon, *Energy Environ. Sci.* **2022**, *15*, 2397–2409.
[44] Y. Kim, S. Park, S.-J. Shin, W. Choi, B. K. Min, H. Kim, W. Kim, Y. J. Hwang, *Energy Environ. Sci.* **2020**, *13*, 4301–4311.
[45] Y. Cao, S. Chen, S. Bo, W. Fan, J. Li, C. Jia, Z. Zhou, Q. Liu, L. Zheng, F. Zhang, *Angew. Chem. Int. Ed.* **2023**, *62*, e202303048.
[46] W. Nie, G. P. Heim, N. B. Watkins, T. Agapie, J. C. Peters, *Angew. Chem. Int. Ed.* **2023**, *62*, e202216102.

Manuscript received: July 2, 2023
Accepted manuscript online: August 28, 2023
Version of record online: September 8, 2023